THE JOURNAL OF PHYSICAL CHEMISTRY C
A JOURNAL OF THE AMERICAN CHEMICAL SOCIETY

pubs.acs.org/JPCC

Article

Robust, Multi-Length-Scale, Machine Learning Potential for Ag−Au Bimetallic Alloys from Clusters to Bulk Materials

Christopher M. Andolina, Marta Bon, Daniele Passerone, and Wissam A. Saidi*

Cite This: *J. Phys. Chem. C* 2021, 125, 17438−17447

Read Online

ACCESS | Metrics & More | Article Recommendations | SI Supporting Information

ABSTRACT: Materials composed of Ag, Au, and Ag−Au alloys remain of great interest despite decades of intense research scrutiny. We interpret these efforts as an impetus for developing robust, accurate, and relatively fast computational methods for modeling these materials. Herein, we describe the training, development, and validation of a machine learning deep neural-network potential (DNP) for improved modeling of Ag−Au systems. This DNP was iteratively trained using density functional theory (DFT) to produce a robust multi-length-scale potential, which yields results comparable to DFT on a wide range of properties such as equilibrium and nonequilibrium lattices, mechanical properties, and defect energies. Further, this DNP can well describe adatom (Ag or Au) energy barriers for diffusion on {100}-, {110}-, and {111}-terminated surfaces (Ag or Au), in agreement with previously reported works. We utilized the DNP to study the nucleation and growth of simulated seeded core−shell Ag and Au nanoparticles (NP). We show that both nanoalloys grow such that {111} facets significantly increase at the expense of the {100} ones. In contrast, the Ag core NP is found to have a more disordered inner structure than the Au one and that Ag adatoms in Au@Ag NP have a more pronounced penetration power than Au in Ag@Au NP. These findings are rationalized in terms of adatom adsorption and diffusion energies.

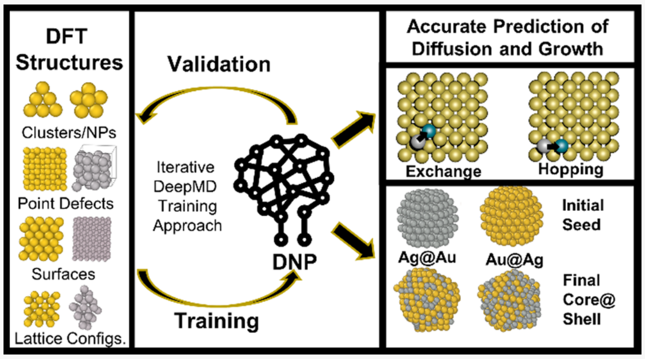

■ INTRODUCTION

Materials composed of Ag, Au, or Ag−Au alloys have been of great interest for many centuries due to their unusual properties, including the resistance to chemical corrosion of Au coins and the array of colloidal Au- and Ag-based pigments in ancient works of art (*e.g.*, the Lycurgus cup[1]), and more recently, the antibacterial properties of Ag materials.[2] Research of Au−Ag materials has explored properties across many length scales from clusters, nanoparticles (NP), thin films of pure metals, and alloys. For instance, Ag−Au clusters and smaller diameter (d < 3 nm) NPs have distinct catalytical[3,4] and photoluminescent[5−8] properties as utilized in different applications;[9−11] Ag−Au NPs with diameters >~3 nm have morphologically tunable localized surface plasmon resonances;[12−14] thin films are used in surface-enhanced Raman spectroscopy applications.[15−17] Computational modeling is an invaluable tool that can minimize bench time and trial-and-error synthetic approach by providing powerful insight into alloying mechanisms, mixing patterns, electron structures, and surface segregation. Such insight will ultimately lead to improved synthetic development and controlled synthesis.[18] Specifically, modeling surface energies and diffusion barriers can provide precise predictions into growth mechanisms.

In 2020, more than 1000 research articles[19] were published investigating Ag, Au, and/or Ag−Au using embedded-atom method (EAM) potentials, thus demonstrating the importance of atomistic calculations and their broad impact across many active areas of material research. Typically, EAM potentials are trained on a mixture of experimental and first-principles results to describe a material's behavior under specific conditions for targeted property considerations. Therefore, each of these EAM potentials has predictive strengths and weaknesses, *e.g.*, trained for clusters, NPs, alloys, high temperature, bulk materials, and/or liquids.[20] Recently, a detailed study compared two atomistic potentials of Zhou et al. (EAM1)[21] and Foiles et al. (EAM2),[22] with density functional theory (DFT), and concluded that the classical potentials could both underestimate/overestimate diffusion barriers during Au−Ag NPs growth.[23]

Research on the development of novel potential functions for metals and alloys has experienced a vast expansion in the last few years, particularly due to the application of modern methods of machine learning (ML) to the creation of transferable and efficient potentials with the accuracy of ab

Received: May 19, 2021
Revised: July 13, 2021
Published: July 29, 2021

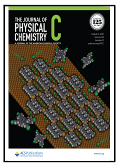

https://doi.org/10.1021/acs.jpcc.1c04403

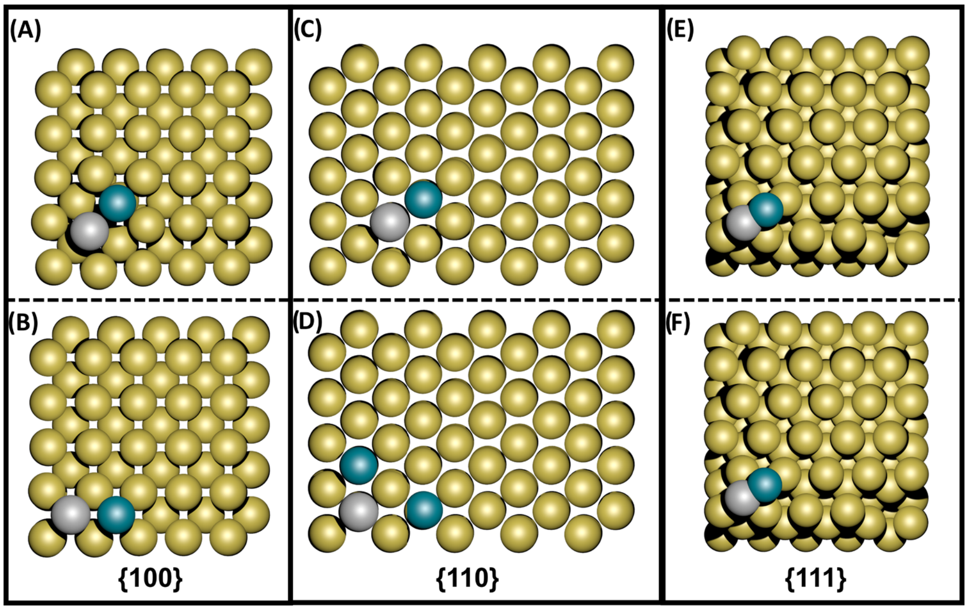

Figure 1. Example surfaces used for the NEB simulations, Ag adatom (silver circle) on Au slabs (gold circle) final position of the Ag adatom (blue circle) for (A) exchange on {100}, (B) {100} hopping, (C) exchange on {110}, (D) SB and LB hopping on {110}, (E) hcp hollow on {111}, and (F) fcc hollow on {111}. Images generated using Atomic Simulation Environment (ASE)[40] software.

initio schemes for the derivation of micro-and macroscopic properties. A recent paper by Rosenbrock et al.[24] demonstrated, for example, the ability of gaussian approximation potential and moment tensor potential, both ML interaction potentials, to reproduce the potential energy surface and properties like the phonon dispersion relation for the bimetallic system Ag−Pd, with DFT accuracy across the entire space of configuration and composition for the solid and liquid space. Less attention is paid to the finite size and surface systems.

Hence, we posit that this is an opportunity to develop a robust multiscale atom-based potential using ML that can produce results with a near-DFT accuracy but with computational costs closer to calculations relying on EAM potential. We employ a deep neural-network potential (DNP), which has the flexibility and nonlinearity necessary to describe various complex potential energy surfaces[25−31] enabling more versatility and broader applications. Most importantly, this DNP potential allows us to readily hone, modify, optimize, and expand the database to account for specific environmental properties with greater ease than an EAM potential (see ref 32).

We developed DNP for the Ag−Au bimetallic alloy system using DeepPot-SE approach[33] as implemented in DeePMD-Kit,[34] and systematically analyzed its fidelity in describing a wide range of properties. Indeed, the suitability of such an approach has been demonstrated in the challenge of structural prediction for bulk systems in Al−Mg intermetallic compounds by Wang et al.[35] We followed an adaptive iterative-learning approach throughout this development to systematically augment the training dataset from regions of the phase space that are not adequately sampled. We further demonstrate that the developed DNP can describe Ag−Au nanoalloys and bulk materials with near-DFT accuracy from cluster to bulk materials. Specifically, we modeled Ag and Au adatoms' diffusion behavior on three different low-index Ag and Au surfaces (Figure 1),[36,37] which are essential for studying Ag−Au deposition and the growth of nanomaterials. We pursue these research efforts to aid in the elucidation of nanomaterial growth, as this topic is an active area of research.[38,39]

■ METHODS

DFT Calculations. The DFT database was generated using the Vienna Ab initio Simulation Package (VASP)[41,42] employing the Perdew−Burke−Ernzerhof (PBE)[43] exchange-correlational functional to solve the Kohn−Sham equations within periodic boundary conditions. As discussed in our previous work,[23] PBE + D3 (van der Waals corrections by Grimme) would provide a better agreement with the experiment than PBE, in particular considering the surface energy ranking between Au and Ag, nevertheless remaining nonquantitative. We decided to utilize PBE in this study so as not to introduce additional empirical parametrization in the standard reference to develop the atomistic potential. Further, PBE is a good compromise between speed and accuracy. A fully quantitative description would require a refinement based on a higher-level functional (*e.g.*, hybrid, meta-GGA) which is not practical at this stage, considering the large data needed to generate the potential. The electron−nucleus interactions are described using the projector augmented wave (PAW) method implemented in VASP[44] using $4d^{10}5s^1$ and $5d^{10}6s^1$ valence configurations for Ag and Au, respectively. Single-particle orbitals are expanded in plane waves generated within a cutoff of 400 eV. We use a dense γ-centered k-grid with a 0.24 $Å^{-1}$ spacing between k-points, equivalent to an $8 \times 8 \times 8$ mesh for bulk Ag/Au with a conventional four atom face-centered cubic (fcc) unit cell. Further, to aid in the k-grid convergence, we use Methfessel−Paxton[45] of order 1 with a 0.15 eV smearing. We terminate the self-consistent electronic loop using a 10^{-8} eV energy-change tolerance to ensure adequate convergence on energies, forces, and virials.

DNP Training Database. To build a general DNP that can describe crystalline and amorphous phases of Ag−Au alloys equally, we constructed a training database that includes bulk, surfaces, and amorphous systems. Model Au−Ag systems are depicted in Figure 1. In total, the database comprises ∼85 k different atomic configurations to ensure that the intrinsically nonphysical form of the ML model has "learned" the relevant physics of the system. Most configurations (∼30 k) are obtained for the small Au−Ag ordered compounds with less than 10 atoms per unit cell after applying different distortions to the system. The total number of Au−Ag slab models is ∼20 k with (100), (111), and (110) orientations employing supercells with 20−80 atoms. The alloy surface configurations are obtained using an fcc lattice with an Ag/Au random occupancy. Also, we augmented the database with ∼5 k random Au−Ag configurations with ∼100 atoms per unit cell generated using Packmol.[46] Further, we included around 15 k NP configurations with less than 100 atoms.

The DFT database was mainly populated from ab initio molecular dynamics (AIMD) trajectories within a constant volume and temperature (NVT) ensemble at a temperature that ranges between 100 and 1500 K. We employed a relatively large 2−4 fs timestep in the AIMD simulations. While this large step could render long AIMD trajectories unstable, it is nevertheless advantageous for the DNP training as it decreases the correlations between the configurations and increases sampling of the relevant phase space.

DNP Model. The DNP was developed using the DeepPot-SE approach[33] as implemented in DeePMD-Kit.[34] As discussed before,[47] we use a cutoff radius of 7 Å for neighbor searching with 2 Å as the smooth cutoff. The maximum number of neighbors within the cutoff radius is set at 200 though a smaller value of ∼100 yields similar accuracy potentials. The dimensions of the embedding and fitting nets are set at 25 × 50 × 100 and 240 × 240 × 240, respectively. The DNP is optimized using Adam stochastic gradient descent method with a learning rate that decreases exponentially from the starting value of 0.001. We used an adaptive-learning loop, which will continue until convergence is met when no extrapolative configurations are found within the selection pool.[47]

Validation of Ag−Au DNP. For the elemental metals, we determine the optimum lattice constants, the energy of cohesion (E_{coh}), defects (point and planar), surface energies, and elastic constants. Further details for specific approaches are found in the Supporting Information. For comparison purposes, we selected two standard Ag−Au EAM atomistic potentials EAM1[21] and EAM2.[22] It should be noted that these EAM potentials were previously used for comparison to DFT diffusion calculations.[23] We utilized the Large-scale Atomic/Molecular Massively Parallel Simulator (LAMMPS, 16 Mar 2018 version)[48] for all of our atomic calculations. Our simulations employed atomic structures that are either constructed using Atomsk,[49] generated in LAMMPS, or downloaded from the Material Project Database (MPDB).[50]

We quantify the errors of the potentials using a simple evaluation of percent differences for different properties with respect to the DFT values. The percent difference (% E_{DIF}) is expressed by eq 1, where E_{DNP} and E_{DFT} are the system's DNP and DFT energies, respectively.

$$\%E_{\mathrm{DIF}} = (E_{\mathrm{DNP}} - E_{\mathrm{DFT}})/E_{\mathrm{DFT}} \times 100 \quad (1)$$

We note that the comparison of the EAM to the DFT values is not on an equal footing to the DNP case, which is solely trained on DFT structures, whereas EAMs are trained on a mixture of theoretical and experimental values. The construction of the validation structures is described in our previous work,[47] and details specific to this work can be found in the SI.

Adatom Adsorption Energies and NEB for Diffusion Barriers. Adsorption sites and diffusion mechanisms on representative surfaces are shown in Figure 1, and the corresponding results are reported in the SI and shown in Figure S1. The adsorption energies (ΔE_{ADS}) were calculated from eq 2:

$$\Delta E_{\mathrm{ADS}} = E - E_{\mathrm{slab}} - E_{\mathrm{atom}} \quad (2)$$

where E is the slab's energy with the atom, E_{slab} is the energy of the slab without the adatom, and E_{atom} is the energy of the isolated atom. Diffusion barriers (ΔE^*) were evaluated via NEB calculations.[51] We used 16 replicas linearly interpolated along the diffusion paths for each NEB trajectory and employed 5 × 5 × 10 slabs for all surfaces and adatom combinations (Figure 1).

Nanoalloy Growth. Following a commonly used computational protocol,[52] we simulated the growth of two different Ag−Au nanoalloys starting from two equilibrated 201-atoms seeds (Ag_{201} and Au_{201}). These were generated via Wulff construction,[53] using surface energies from the literature.[23] The two seeds correspond to truncated octahedrons, exposing {100} and {111} facets. Simulations were run in the gas phase employing NVT ensemble and a velocity rescaling thermostat[54] set at T = 297 K. The timestep for integrating Newton's equations of motion was set to 4 fs. Adatoms were deposited on the thermalized seeds every 2 ps while allowing all atoms to freely move between two subsequent depositions. We quantified the chemical ordering of the nanoalloy using the radial distribution functions from the seed center.[55] Further, we analyzed the atomic migration toward the outer shell or adatom penetration using common-neighbor analysis.[55] We would like to emphasize that these growth simulations are for illustrative purposes, and to prove the reliability of the developed DNP model, by comparing some among the predicted configurations (not included in the initial training) with DFT predictions. To deeply explore Au−Ag NP growth, one should test different simulation conditions, *e.g.*, different seed shapes, deposition rates, and temperature. These aspects will be the subject of a future investigation.

■ RESULTS AND DISCUSSION

We first report on the validation of the Au−Ag DNP model, which not only describes the binary alloys but pure bulk Ag and Au phases as well. For each metal (Ag or Au), we compare our DNP-derived values to known DFT values for lattice parameter (fcc, bcc, sc, diamond, hcp) and cohesive energy (E_{coh}), point defects (vacancies and interstitial atoms), elastic constants (bulk modulus, Young's modulus, shear modulus, and Poisson's ratio), 2D and 3D cluster structures (n = 6−9 atoms), surface energies of different terminations (Miller indices less than 4) and planar defects, calumniating in a total of 56 validated properties for each bulk metal (Ag and Au), respectively. We quantify the potentials' difference using a simple evaluation eq 1 of the percent difference with the DFT values.

Lattice Constants, Energy of Cohesion, Elastic Constants. Accurate modeling of a material's mechanic properties is a fundamental first step in validating new potential and an area where EAM potentials have been demonstrated to perform well compared with DFT and experimental results. The lattice constants, energies of cohesion (E_{coh}), elastic constants, and calculated moduli are listed in Table 1 for Ag and Table 2 for Au. Additional Ag and Au benchmarks for bulk point defects (Table S1), cluster energies (Table S2), and non-ground-state lattices (Table S3) are listed with comparisons to EAM1 and EAM2, in the SI.

Table 1. Experimental, EAM, DNP, and DFT Mechanical Properties of Bulk Ag[a]

property	EXP	DNP	EAM1	EAM2	DFT[50]
fcc a	4.07[56]	4.15	4.09	4.09	4.15
fcc E_{coh}	−2.85[57]	−2.71	−2.85	−2.85	−2.83
V_0 (Å^3/atom)	16.9	17.9	17.0	17.0	18.0
C_{11}	132[58]	115	129	143	100
C_{12}	97[58]	88	91	150	82
C_{44}	51[58]	44	57	35	41
bulk modulus (K_H)	100[58]	97	104	148	88
shear modulus (G_H)	30[58]	32	42	20	28
Young's modulus (E_H)	83[58]	86	110	56	57
Poisson's ratio (ν)	0.37[58]	0.35	0.32	0.44	0.38

[a] Lattice constants (a) are in Å, E_{coh} in eV/atom, and elastic constants and moduli in GPa. EXP V_0 and DFT E_H were calculated from the measured literature values for comparison. K_H, G_H, and E_H are the bulk modulus, shear modulus, and Young's modulus defined by Hill (see the SI for all equations).[59−61]

Table 2. Experimental, EAM, DNP, and DFT Mechanical Properties of Bulk fcc Au[a]

property	EXP	DNP	EAM1	EAM2	DFT[50]
fcc a	4.07[62]	4.16	4.08	4.04	4.17
fcc E_{coh}	−3.93[57]	−3.22	−3.93	−3.93	−3.27
V_0 (Å^3/atom)	16.9	18.0	17.0	17.0	18.2
C_{11}	193[58]	170	165	186	144
C_{12}	163[58]	138	131	157	134
C_{44}	42[58]	36	33	42	29
bulk modulus (K_H)	180[58]	149	143	167	137
shear modulus (G_H)	27[58]	28	27	31	19
Young's modulus (E_H)	173[58]	79	75	88	89
Poisson's ratio (ν)	0.42[58]	0.41	0.41	0.41	0.45

[a] Units and symbols are defined in Table 1 footnote.

Free Surfaces Energies for Low-Index Ag and Au Surfaces. We modeled Ag- and Au-terminated surfaces identified by low Miller indices (never larger than 3) as some larger NPs have highly faceted surfaces; therefore, further enhancing the importance of accurately modeling these surface energies. These slab models are constructed using the optimized lattice constants by orienting the surface perpendicular to the z-axis and doubling the simulation box's z length to add a vacuum in the nonperiodic direction to mitigate spurious interactions. The surface energies are reported in Table 3 (see Tables S4 and S5 for EAM1 and EAM2 results, respectively). We obtained similar surface energy values using either the direct or the Fiorentini−Methfessel method.[63] As seen from Table 3, for the Ag and Au surfaces, the surfaces follow the correct order of increasing surface energies {111} < {100} < {110}. We also highlight our DNP results' excellent agreement with the DFT values obtained from MPDB[50] as the percent difference is lower than 9%.

Table 3. Surface Energies γ_s in (mJ/m^2) for Ag and Au Slabs

	γ_s Ag			γ_s Au		
surface termination	DNP	DFT	% E_{DIFF}	DNP	DFT	% E_{DIFF}
100	821	820	<1	835	860	3
110	871	870	<1	855	830	3
111	695	760	9	648	710	9
210	940	900	5	895	910	2
211	843	879	4	818	820	<1
221	829	820	1	752	780	4
310	925	890	4	898	910	1
311	877	860	2	834	870	4
320	931	890	5	881	910	3
321	880	860	3	827	850	3
322	809	770	5	736	750	2
331	857	850	1	791	830	5
332	801	790	1	722	750	4

Planar Defects. Planar defects are common structures found in Au and Ag monometallic nanosystems. In particular, twin boundaries are significant growth-directing defects for anisotropic NPs, which significantly impacts the resulting morphologies (*e.g.*, Au nanoprisms, Au/Ag nanorods).[64−67] Although we did not include these structures in our DNP training, we found that we can predict the DFT energies of these defects relatively well (Table 4). We observe less agreement for the Au planar defects, which indicates that more training is needed to better describe these properties. Nevertheless, we observe similar accuracy compared to EAM1 and EAM2 (Tables S6 and S7). We also note that this current version of the DNP fails to accurately describe the (111) twin plane energy compared to DFT values. In summary, the DFT agreement on most planar defects is an excellent demonstration of the DNP ability to interpolate structures in the training set.

Diffusion on {100} Surfaces. Our results confirm previous findings by Bon et al.[23] as we observe that the Au adatoms have larger adsorption energy (ΔE_{ADS}) than Ag (Table 5) compared to the same slab surface, as predicted previously. We also note that an adatom has lower ΔE_{ADS} on a slab with the same chemical identity (Table 5), *e.g.*, Au on an Au slab is of lower energy (3.30 eV) than Au on a Ag slab (3.36 eV). Diffusion is initiated with Ag and/or Au adsorption process on clean {100} surfaces at hollow sites only,[23,68,69] followed by hopping or exchange diffusion (Figure 1). The NEB energy barriers for each adatom on each {100} slab are shown in Figure 2.

The hetero-adsorption diffusion, Ag on a Au slab and Au on a Ag slab, favors an exchange mechanism $\Delta E_{EX}* < \Delta E_{Hop}*$, where ΔE_{EX} is the barrier energy to exchange the adatom with a surface atom and Hop is the barrier for the adatom to move to a new hollow site. This smaller barrier to exchange suggests a favorability of mixing coupled with $\Delta E_{EX} < \Delta E_{ADS}$ for heteroatom systems. The adatom energetically favors incorporation into the slab surface rather than diffusion across the surface, consistent with the literature.[23,70,71]

Diffusion on {110} Surfaces. As shown in Figure 1, the diffusion path on {110} slabs is complicated, as the Ag and Au adatoms that occupy hollow sites have four competing diffusion mechanisms/pathways (Figure 3), namely, short-bridge (ΔE_{SB}), long-bridge (ΔE_{LB}), or cross-channel diffusion via adatom exchange.[23,69,72]

For both Ag and Au {110} surfaces, the adsorption energies after the in-channel hetero-adsorption (ΔE_{EX}) are higher compared to adsorption at the hollow site (ΔE_{ADS}), as was also observed by DFT[23] (Tables 5 and 6). We note that the

Table 4. Ag and Au Planar Defects Surface Energies (mJ/m^2) Compared to DFT[a]

				γ_s Ag			γ_s Au		
sigma	defect plane	rotation plane	rotation	DNP	DFT	% E_{DIFF}	DNP	DFT	% E_{DIFF}
3	$1\overline{12}$	110	180.0	362	430	16	603	460	31
3	$1\bar{1}0$	111	109.5	586	540	8.6	254	340	25
3	111	111	60.0	8	70	88	74	30	150
5	$0\overline{13}$	100	53.1	491	550	11	499	450	11
5	$0\bar{2}1$	100	36.9	531	590	10	493	520	4.4
5	100	100	36.9	407	420	3.0	352	320	9.8
7	111	111	36.9	183	210	13	404	440	8.3
7	$3\overline{21}$	111	38.2	514	540	4.6	181	170	6.3
9	110	110	38.9	458	510	10	412	390	5.5
9	$2\overline{21}$	110	38.9	677	710	4.7	613	610	<1

[a]Notably, the DNP training dataset did not include similar defects.

Table 5. Adsorption Energy and Diffusion Barriers (eV) for Adatoms on the {100} Surface

slab	adatom	property	DNP	PBE[23]	% E_{DIFF}
Ag	Ag	ΔE_{ADS}	2.55	2.37	8
		ΔE_{Hop}[a]	0.42	0.46	8
		ΔE_{EX}[a]	0.39	0.52	26
	Au	ΔE_{ADS}	3.36	2.99	12
		ΔE_{EX}	2.97	3.02	2
		ΔE_{Hop}[a]	0.64	0.55	15
		ΔE_{EX}[a]	0.37	0.43	15
Au	Ag	ΔE_{ADS}	2.79	2.70	3
		ΔE_{EX}	2.59	2.88	10
		ΔE_{Hop}[a]	0.41	0.53	21
		ΔE_{EX}[a]	0.16	0.19	16
	Au	ΔE_{ADS}	3.30	3.06	8
		ΔE_{Hop}[a]	0.57	0.61	7
		ΔE_{EX}[a]	0.12	0.11	5

[a]indicates NEB barrier.

diffusion short-bond hop (ΔE_{SB}*) is the most favorable mechanism for all adatoms on either Au or Ag slab, excluding Au adatoms on an Au slab that slightly favor an ΔE_{EX}*. Our results suggest that adatoms on the {110} surface will preferentially diffuse via a ΔE_{SB}* mechanism. Although the barrier for ΔE_{EX}* is only ~0.03 eV larger than ΔE_{SB}* for most of these systems (excluding Ag on Au slab with a 0.13 eV difference), which may suggest another available albeit a less probable diffusion pathway for these adatoms on the {110} surface.

Diffusion on {111} Surfaces. The two adatoms binding sites show that the fcc (fcc hollow) and hcp (hcp hollow) are nearly equal in energy (ΔE_{fcc} and ΔE_{hcp}), which have similar adsorption energies (Figure 4, Table 7) consistent with the literature.[23] We also observe a trend of higher Au adatom adsorption energy than Ag, which is also observed for both adatoms on the {100} and {110} surfaces. However, we note a difference in the trend of the adatom adsorption energies for the {111} surface, where we observe that the adsorption of adatoms on the Ag surface is more favorable than the Ag surface. Due to the low barrier of ΔE_{Hop}* for all systems on {111}, the diffusion from fcc to hcp or hcp to fcc hollow are nearly equal in energy, which suggests that diffusion of the adatom (Ag or Au) on the {111} surface (Ag or Au slab) from the hollow site (hcp or fcc) is the favored mechanism, consistent with experimental and theoretical observations in the literature.[23,55,73,74]

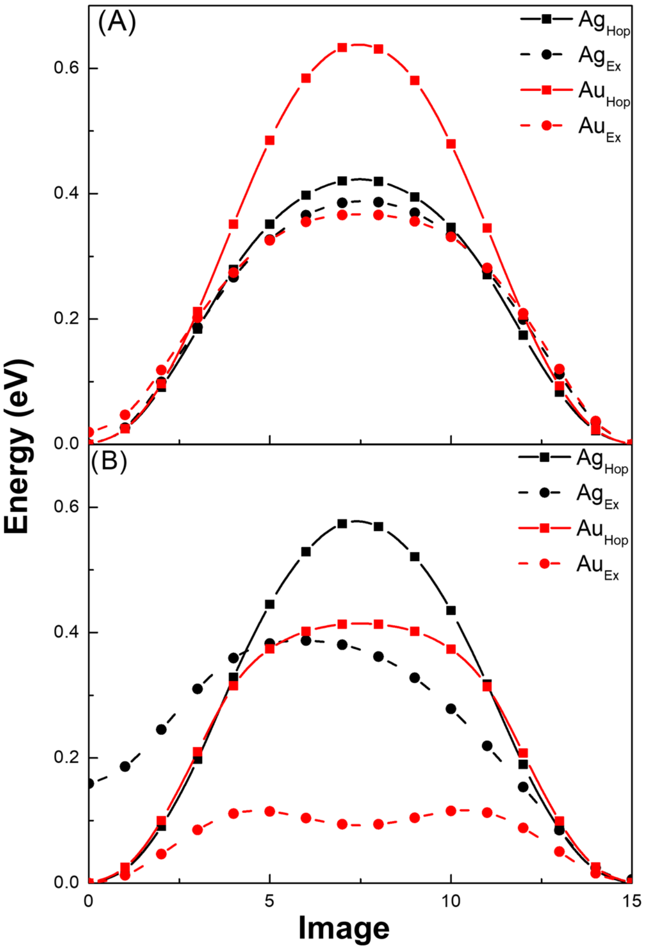

Figure 2. NEB energy barrier plot showing the system energy for both adatoms along the diffusion pathway on a {100} slab for (A) Ag and (B) Au surface slabs. Lines are added to guide the eye.

Taken together, we observe good agreement with the previously reported DFT-PBE literature values (Tables 5–7). However, note that some of the deviations (% E_{DIFF}) from the literature values are smaller than others, e.g., in Table 5 for Ag adatoms on a Ag slab ΔE_{Hop}* and ΔE_{EX}* are 8 and 26%, respectively. These differences are likely due to a combination of factors such as different DFT simulation codes were used in these studies (VASP and QUANTUM-ESPRESSO[74]), or different computational frameworks. Additionally, the DNP values may over- or underestimate the energies as noted before

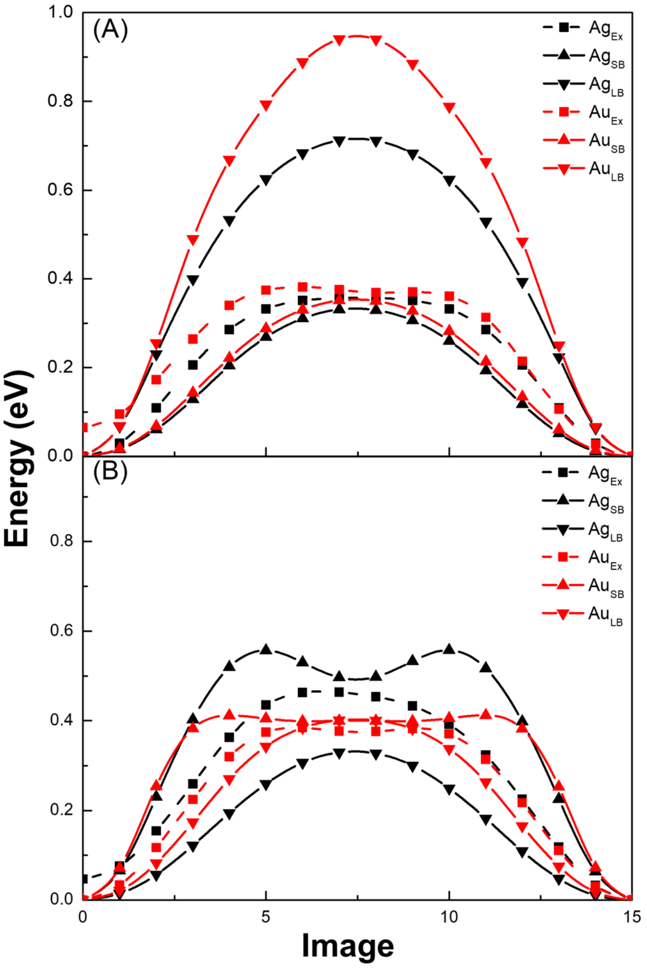

Figure 3. NEB energy barrier plot shows the system energy for both adatoms along the diffusion pathway {110} slab for (A) Ag and (B) Au slabs. Lines are added to guide the eye.

Table 6. Adsorption Energy and Diffusion Barriers (eV) for Adatoms on the {110} Surface

slab	adatom	property	DNP	PBE[13]	% E_{DIFF}
Ag	Ag	ΔE_{ADS}	2.28	2.47	8
		ΔE_{LB}[a]	0.71	0.73	2
		ΔE_{SB}[a]	0.33	0.36	8
		ΔE_{EX}[a]	0.36	0.37	3
	Au	ΔE_{ADS}	3.30	3.14	5
		ΔE_{EX}	3.39	3.05	11
		ΔE_{LB}[a]	0.94	0.77	22
		ΔE_{SB}[a]	0.35	0.44	20
		ΔE_{EX}[a]	0.38	0.41	7
Au	Ag	ΔE_{ADS}	2.50	2.53	1
		ΔE_{EX}	2.55	2.81	9
		ΔE_{LB}[a]	0.56	0.69	19
		ΔE_{SB}[a]	0.33	0.38	13
		ΔE_{EX}[a]	0.46	0.44	5
	Au	ΔE_{ADS}	3.00	2.93	2
		ΔE_{LB}[a]	0.41	0.66	38
		ΔE_{SB}[a]	0.40	0.45	11
		ΔE_{EX}[a]	0.38	0.48	20

[a] indicates NEB barrier.

when comparing the DFT-PBE results to available EAM potentials.

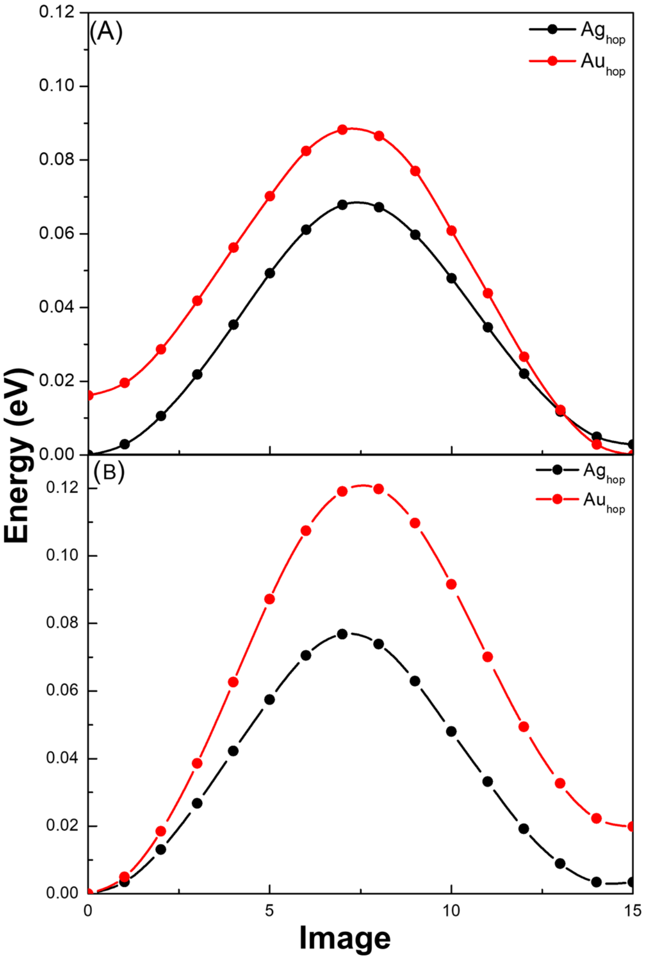

Figure 4. NEB energy barrier plot showing the system energy for both adatoms along the diffusion pathway on (A) Ag {111} and (B) Au {111} surface slabs. Lines are added to guide the eye.

Table 7. Adsorption Energy and Diffusion Barriers (eV) for Adatoms on the {111} Surface

slab	adatom	property	DNP	PBE[13]	% E_{DIFF}
Ag	Ag	ΔE_{fcc}	1.64	2.16	24
		ΔE_{hcp}	1.64	2.16	24
		ΔE_{Hop}[a]	0.06	0.06	7
	Au	ΔE_{fcc}	2.13	2.68	21
		ΔE_{hcp}	2.14	2.68	20
		ΔE_{Hop}[a]	0.09	0.08	17
Au	Ag	ΔE_{fcc}	1.83	2.07	12
		ΔE_{hcp}	1.83	2.07	12
		ΔE_{Hop}[a]	0.08	0.08	4
	Au	ΔE_{fcc}	2.31	2.31	<1
		ΔE_{hcp}	2.31	2.30	<1
		ΔE_{Hop}[a]	0.12	0.11	8

[a] indicates NEB barrier.

Comparison of Surfaces. When comparing the adatom energies across the surfaces, we notice trends consistent for slab and adatom regardless of chemical identity. For both slabs, the energies of the adatom adsorption energies (both $\Delta E_{\mathrm{ADS,Ag}}$ and $\Delta E_{\mathrm{ADS,Au}}$) follow {110} > {100} > {111}. Previous DFT (PBE) results indicated a similar trend with the exclusion of Ag on an Au slab showing {100} > {110} > {111}.[23] Note that, in general, we do observe modestly improved DNP accuracy with the DFT {100} and {110} surfaces than with the {111} surface. However, this energy difference may be ascribed to the differences between the computational setup employed in constructing the DNP training datasets and those employed in the DFT PBE calculations.

Nanoalloy Growth. After showing that the DNP can accurately describe adsorption energies and diffusion events on surfaces of different orientations, we next apply it to study the growth of Ag−Au nanoalloys starting from Ag and Au seeds (Figure 5). Consistent with previous theoretical studies,[23,75] we find for both seeds that the {111} facets significantly increase in size, at the expense of the {100} surfaces that are progressively disappearing during the nanoalloy growth process. This behavior can be explained based on diffusion barriers on corresponding terraces. Namely, as reported in Tables 5−7, diffusion from {111} Ag/Au surfaces is the fastest (*i.e.*, associated with the lowest potential energy barrier) among all of the interface diffusion processes. As a result, the nanoalloy tends to be octahedral in shape, as seen in Figure 5A. However, we note that adatom crossing from (111) to (100) is faster than (100) to (111), which results in the apparent trapping of adatoms on the (100) facets.[76] For this validation, the favorable comparison of DNP energies against DFT for selected configurations from the trajectory shown in Figure S2 indicates that the DNP can well describe this process.

Growth simulations allow us to estimate phenomena like order/disorder, alloying, and penetration of adatoms (with simultaneous migration from the core to the surface) as a function of the deposited atoms. For both nanoclusters, adatoms diffusion is limited within the outer shells, generating a core−shell structure (cross sections in Figure 5B) in line with experimental evidence.[23,77] Nevertheless, a more disordered core structure is observed for the $\mathrm{Ag_{201}@Au_{201}}$ NP than for the Au-seed NP. This is evidenced by analyzing the radial distribution function, $\rho_{\mathrm{Ag\ Au}}$, that measures the distribution of the atoms from the center of the seed (eq 3).

$$\rho_{\mathrm{Ag\ Au}}(r) = \frac{n_{\mathrm{Ag\ Au}}(r)}{4\pi r^2 \Delta r} \qquad (3)$$

Here, $n_{\mathrm{Ag\ Au}}(r)$ is the number of atoms of the two species in a shell at a distance between r and $r + \Delta r$. As seen in Figure 5B, the interseparation of the inner peaks is less sharp (more disordered inner structure) for the Ag than for the Au core atoms. We stress the importance of the simulation to shed light on this structural aspect because such information is easy to measure for bulk materials (via diffraction measurements) but difficult to capture in physical experiments for this length scale.[55,73,78]

Further, we examined the distribution of the atoms during deposition to quantify the core-atom migration to the outer shell. To distinguish between atoms belonging to the surface and the core, we relied on coordination number (CN) analysis. Namely, atoms belonging to the surface have—by definition—a lower number of first neighbors. In this CNN analysis, the nearest neighbors' cutoff distance was set to 3.65 Å, and atoms with CN = 12 were considered inside the NP. As is clear from Figure 5C, a more pronounced penetration power of the Ag adatoms in the Au201@Ag201 NP than Au in the Ag201@Au201 NP (Figure 5) into the NP core is observed. These results are consistent with the hetero-adsorption energies of Table 6 that is the first step toward diffusion toward the NP core. Namely, in Table 6, we showed larger adsorption energies of Ag on Au {111} and {100} compared to the ones of Au adatoms on the same Miller index Ag surfaces.

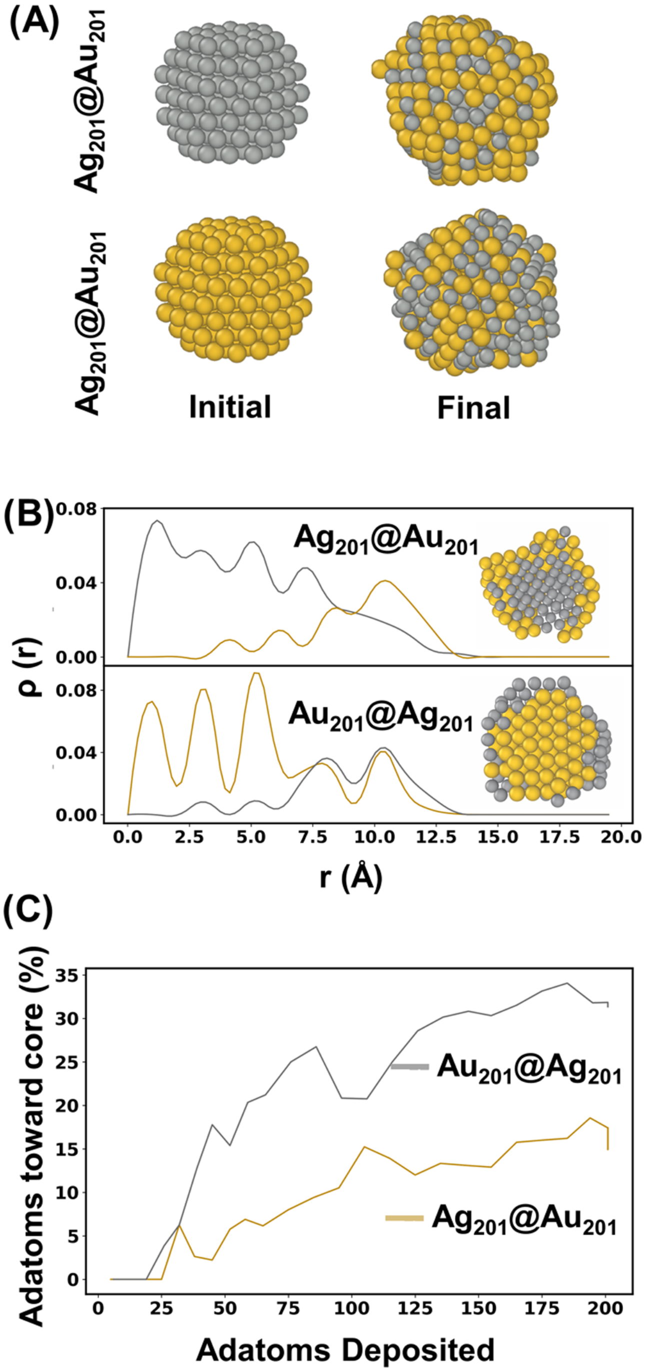

Figure 5. Simulated seeded core−shell growth on Ag and Au NPs using the DNP. (A) Initial and final configurations of the simulated NPs. (B) Radial distribution functions as obtained from eq 3 of the last 5 equilibrated ns of the NP as a function of the distance r from the NP center. (Top) $\mathrm{Ag_{201}@Au_{201}}$, (bottom) $\mathrm{Au_{201}@Ag_{201}}$. In silver, Ag atoms, and gold, Au adatoms distributions. (C) Percentage of atoms deposited migrating inside the NP. The gold curve is associated with $\mathrm{Ag_{201}@Au_{201}}$, while the silver one with $\mathrm{Au_{201}@Ag_{201}}$.

■ CONCLUSIONS

We have developed an atomistic potential based on deep neural networks using the DeepPot-SE approach for the Au−Ag system. Our DNP was validated against DFT values we trained on and other properties that DNP was not explicitly trained on, such as bulk Ag and Au planar defects. Overall, we found that DNP is robust for calculating Ag−Au properties from molecular clusters to bulk materials. Furthermore, our DNP potential can reproduce DFT PBE approach benchmarks for modeling the diffusion of adatoms on clean {100}-, {110}-, and {111}-terminated surfaces and is likely a good descriptor of nanoscale diffusion processes for Au−Ag NPs. The growth simulations of $Ag_{201}@Au_{201}$ and $Au_{201}@Ag_{201}$ results are consistent with previous theoretical and experimental observations, as we observe core−shell structures to grow in both simulations. Ultimately, this work will help accelerate the understanding and controlled synthesis of Ag−Au nanoalloys. Also, this approach is readily adaptable to other bimetallic systems allowing for systematic explorations.

■ ASSOCIATED CONTENT

Supporting Information

The Supporting Information is available free of charge at https://pubs.acs.org/doi/10.1021/acs.jpcc.1c04403.

> Comparison of validation properties to EAM point defects, details regarding the calculation of nontypical lattice configurations, NEB energy barrier plots, equations for elastic constant calculations, energies of planar surfaces and defects, and comparison of DNP and DFT NP growth. The training database and the potential are freely available at saidigroup.pitt.edu or by contacting the corresponding author (PDF)

■ AUTHOR INFORMATION

Corresponding Author

Wissam A. Saidi − *Department of Mechanical Engineering and Materials Science, University of Pittsburgh, Pittsburgh, Pennsylvania 15216, United States;* orcid.org/0000-0001-6714-4832; Email: alsaidi@pitt.edu

Authors

Christopher M. Andolina − *Department of Mechanical Engineering and Materials Science, University of Pittsburgh, Pittsburgh, Pennsylvania 15216, United States;* orcid.org/0000-0003-2157-9114

Marta Bon − *Empa, Swiss Federal Laboratories for Materials Science and Technology, Electron Microscopy Center, CH-8600 Dübendorf, Switzerland;* Present Address: CRUK Beatson Research Institute, University of Scotland, Glasgow G61 1BD, United Kingdom; orcid.org/0000-0002-9930-7728

Daniele Passerone − *Empa, Swiss Federal Laboratories for Materials Science and Technology, Electron Microscopy Center, CH-8600 Dübendorf, Switzerland*

Complete contact information is available at: https://pubs.acs.org/10.1021/acs.jpcc.1c04403

Notes

The authors declare no competing financial interest.
The manuscript was written through the contributions of all authors. All authors have given approval to the final version of the manuscript.

■ ACKNOWLEDGMENTS

The authors are grateful to the US National Science Foundation (Award no. CSSI-2003808). They are also grateful for computing time provided in part by the Pittsburgh Center for Research Computing (CRC) resources at the University of Pittsburgh, Extreme Science and Engineering Discovery Environment (XSEDE), which is supported by the National Science Foundation (NSF OCI-1053575) and Argonne Leadership Computing Facility, which is a DOE Office of Science User Facility supported under Contract DE-AC02-06CH11357.

■ REFERENCES

(1) Freestone, I.; Meeks, N.; Sax, M.; Higgitt, C. The Lycurgus Cup—a Roman Nanotechnology. *Gold Bull.* **2007**, *40*, 270−277.

(2) Möhler, J. S.; Sim, W.; Blaskovich, M. A. T.; Cooper, M. A.; Ziora, Z. M. Silver Bullets: A New Lustre on an Old Antimicrobial Agent. *Biotechnol. Adv.* **2018**, *36*, 1391−1411.

(3) Zhao, J.; Jin, R. Heterogeneous Catalysis by Gold and Gold-Based Bimetal Nanoclusters. *Nano Today* **2018**, *18*, 86−102.

(4) Astruc, D. Introduction: Nanoparticles in Catalysis. *Chem. Rev.* **2020**, *120*, 461−463.

(5) Grandjean, D.; Coutiño-Gonzalez, E.; Cuong, N. T.; Fron, E.; Baekelant, W.; Aghakhani, S.; Schlexer, P.; D'Acapito, F.; Banerjee, D.; Roeffaers, M. B.; et al. Origin of the Bright Photoluminescence of Few-Atom Silver Clusters Confined in Lta Zeolites. *Science* **2018**, *361*, 686−690.

(6) Andolina, C. M.; Dewar, A. C.; Smith, A. M.; Marbella, L. E.; Hartmann, M. J.; Millstone, J. E. Photoluminescent Gold-Copper Nanoparticle Alloys with Composition-Tunable near-Infrared Emission. *J. Am. Chem. Soc.* **2013**, *135*, 5266−9.

(7) Huang, T.; Murray, R. W. Visible Luminescence of Water-Soluble Monolayer-Protected Gold Clusters. *J. Phys. Chem. B* **2001**, *105*, 12498−12502.

(8) Huang, T.; Murray, R. W. Luminescence of Tiopronin Monolayer-Protected Silver Clusters Changes to That of Gold Clusters Upon Galvanic Core Metal Exchange. *J. Phys. Chem. B* **2003**, *107*, 7434−7440.

(9) Shang, L.; Dong, S.; Nienhaus, G. U. Ultra-Small Fluorescent Metal Nanoclusters: Synthesis and Biological Applications. *Nano Today* **2011**, *6*, 401−418.

(10) Medina-Cruz, D.; Saleh, B.; Vernet-Crua, A.; Nieto-Argüello, A.; Lomelí-Marroquín, D.; Vélez-Escamilla, L. Y.; Cholula-Díaz, J. L.; García-Martín, J. M.; Webster, T. Bimetallic Nanoparticles for Biomedical Applications: A Review. In *Racing for the Surface*; Springer, 2020; pp 397−434.

(11) Bhatia, E.; Banerjee, R. Hybrid Silver-Gold Nanoparticles Suppress Drug Resistant Polymicrobial Biofilm Formation and Intracellular Infection. *J. Mater. Chem. B* **2020**, *8*, 4890−4898.

(12) Yang, Y.; Liu, J.; Fu, Z. W.; Qin, D. Galvanic Replacement-Free Deposition of Au on Ag for Core-Shell Nanocubes with Enhanced Chemical Stability and Sers Activity. *J. Am. Chem. Soc.* **2014**, *136*, 8153−6.

(13) Chowdhury, A. D.; Nasrin, F.; Gangopadhyay, R.; Ganganboina, A. B.; Takemura, K.; Kozaki, I.; Honda, H.; Hara, T.; Abe, F.; Park, S.; et al. Controlling Distance, Size and Concentration of Nanoconjugates for Optimized Lspr Based Biosensors. *Biosens. Bioelectron.* **2020**, *170*, No. 112657.

(14) Sato, R.; Ohnuma, M.; Oyoshi, K.; Takeda, Y. Experimental Investigation of Nonlinear Optical Properties of Ag Nanoparticles: Effects of Size Quantization. *Phys. Rev. B* **2014**, *90*, No. 125417.

(15) Maurer, T.; Nicolas, R.; Lévêque, G.; Subramanian, P.; Proust, J.; Béal, J.; Schuermans, S.; Vilcot, J.-P.; Herro, Z.; Kazan, M.; et al. Enhancing Lspr Sensitivity of Au Gratings through Graphene Coupling to Au Film. *Plasmonics* **2014**, *9*, 507−512.

(16) Sun, F.; Galvan, D. D.; Jain, P.; Yu, Q. Multi-Functional, Thiophenol-Based Surface Chemistry for Surface-Enhanced Raman Spectroscopy. *Chem. Commun.* **2017**, *53*, 4550−4561.

(17) Saito, Y.; Wang, J.; Smith, D.; Batchelder, D. A Simple Chemical Method for the Preparation of Silver Surfaces for Efficient Sers. *Langmuir* **2002**, *18*, 2959−2961.

(18) Ferrando, R.; Jellinek, J.; Johnston, R. L. Nanoalloys: From Theory to Applications of Alloy Clusters and Nanoparticles. *Chem. Rev.* **2008**, *108*, 845−910.

(19) Google Scholar Search of: "Embedded Atom Method" or Au or Ag or Ag-Au.

(20) Rassoulinejad-Mousavi, S. M.; Zhang, Y. Interatomic Potentials Transferability for Molecular Simulations: A Comparative Study for Platinum, Gold and Silver. *Sci. Rep.* **2018**, *8*, No. 2424.

(21) Zhou, X. W.; Johnson, R. A.; Wadley, H. N. G. Misfit-Energy-Increasing Dislocations in Vapor-Deposited Cofe/Nife Multilayers. *Phys. Rev. B* **2004**, *69*, No. 144113.

(22) Foiles, S. M.; Baskes, M. I.; Daw, M. S. Embedded-Atom-Method Functions for the Fcc Metals Cu, Ag, Au, Ni, Pd, Pt, and Their Alloys. *Phys. Rev. B* **1986**, *33*, 7983−7991.

(23) Bon, M.; Ahmad, N.; Erni, R.; Passerone, D. Reliability of Two Embedded Atom Models for the Description of Ag@ Au Nanoalloys. *J. Chem. Phys.* **2019**, *151*, No. 064105.

(24) Rosenbrock, C. W.; Gubaev, K.; Shapeev, A. V.; Pártay, L. B.; Bernstein, N.; Csányi, G.; Hart, G. L. W. Machine-Learned Interatomic Potentials for Alloys and Alloy Phase Diagrams. *Npj Comput. Mater.* **2021**, *7*, No. 24.

(25) Lorenz, S.; Groß, A.; Scheffler, M. Representing High-Dimensional Potential-Energy Surfaces for Reactions at Surfaces by Neural Networks. *Chem. Phys. Lett.* **2004**, *395*, 210−215.

(26) Sumpter, B. G.; Noid, D. W. Potential Energy Surfaces for Macromolecules. A Neural Network Technique. *Chem. Phys. Lett.* **1992**, *192*, 455−462.

(27) Manzhos, S.; Dawes, R.; Carrington, T. Neural Network-Based Approaches for Building High Dimensional and Quantum Dynamics-Friendly Potential Energy Surfaces. *Int. J. Quantum Chem.* **2015**, *115*, 1012−1020.

(28) Manzhos, S.; Carrington, T., Jr. A Random-Sampling High Dimensional Model Representation Neural Network for Building Potential Energy Surfaces. *J. Chem. Phys.* **2006**, *125*, No. 084109.

(29) Bartók, A. P.; Payne, M. C.; Kondor, R.; Csanyi, G. Gaussian Approximation Potentials: The Accuracy of Quantum Mechanics, without the Electrons. *Phys. Rev. Lett.* **2010**, *104*, No. 136403.

(30) Behler, J.; Parrinello, M. Generalized Neural-Network Representation of High-Dimensional Potential-Energy Surfaces. *Phys. Rev. Lett.* **2007**, *98*, No. 146401.

(31) Chmiela, S.; Sauceda, H. E.; Muller, K. R.; Tkatchenko, A. Towards Exact Molecular Dynamics Simulations with Machine-Learned Force Fields. *Nat. Commun.* **2018**, *9*, No. 3887.

(32) Andolina, C. M.; Williamson, P.; Saidi, W. A. Optimization and Validation of a Deep Learning Cuzr Atomistic Potential: Robust Applications for Crystalline and Amorphous Phases with near-Dft Accuracy. *J. Chem. Phys.* **2020**, *152*, No. 154701.

(33) Zhang, L.; Han, J.; Wang, H.; Saidi, W. A.; Car, R.; E, W. In *End-to-End Symmetry Preserving Inter-Atomic Potential Energy Model for Finite and Extended Systems*, Advances in Neural Information Processing Systems 31, Bengio, S.; Wallach, H.; Larochelle, H.; Grauman, K.; Cesa-Bianchi, N.; Garnett, R., Eds.; Curran Associates, Inc., 2018; pp 4441−4451.

(34) Wang, H.; Zhang, L.; Han, J.; Weinan, E. Deepmd-Kit: A Deep Learning Package for Many-Body Potential Energy Representation and Molecular Dynamics. *Comput. Phys. Commun.* **2018**, *228*, 178−184.

(35) Wang, H.; Zhang, Y.; Zhang, L.; Wang, H. Crystal Structure Prediction of Binary Alloys Via Deep Potential. *Front. Chem.* **2020**, *8*, No. 589795.

(36) Baletto, F.; Mottet, C.; Ferrando, R. Growth of Three-Shell Onionlike Bimetallic Nanoparticles. *Phys. Rev. Lett.* **2003**, *90*, No. 135504.

(37) Müller, M.; Albe, K. Lattice Monte Carlo Simulations of Fept Nanoparticles: Influence of Size, Composition, and Surface Segregation on Order-Disorder Phenomena. *Phys. Rev. B* **2005**, *72*, No. 094203.

(38) Nelli, D.; Roncaglia, C.; Ahearn, S.; Di Vece, M.; Ferrando, R.; Minnai, C. Octahedral Growth of Ptpd Nanocrystals. *Catalysts* **2021**, *11*, 718.

(39) Xia, Y.; Nelli, D.; Ferrando, R.; Yuan, J.; Li, Z. Shape Control of Size-Selected Naked Platinum Nanocrystals. *Nat. Commun.* **2021**, *12*, No. 3019.

(40) Larsen, A. H.; Mortensen, J. J.; Blomqvist, J.; Castelli, I. E.; Christensen, R.; Dułak, M.; Friis, J.; Groves, M. N.; Hammer, B.; Hargus, C. The Atomic Simulation Environment—a Python Library for Working with Atoms. *J. Phys.: Condens. Matter* **2017**, *29*, No. 273002.

(41) Kresse, G.; Furthmuller, J. Efficient Iterative Schemes for Ab Initio Total-Energy Calculations Using a Plane-Wave Basis Set. *Phys. Rev. B* **1996**, *54*, No. 11169.

(42) Shishkin, M.; Marsman, M.; Kresse, G. Accurate Quasiparticle Spectra from Self-Consistent Gw Calculations with Vertex Corrections. *Phys. Rev. Lett.* **2007**, *99*, No. 246403.

(43) Perdew, J. P.; Burke, K.; Ernzerhof, M. Generalized Gradient Approximation Made Simple. *Phys. Rev. Lett.* **1996**, *77*, No. 3865.

(44) Kresse, G.; Joubert, D. From Ultrasoft Pseudopotentials to the Projector Augmented-Wave Method. *Phys. Rev. B* **1999**, *59*, 1758.

(45) Methfessel, M.; Paxton, A. T. High-Precision Sampling for Brillouin-Zone Integration in Metals. *Phys. Rev. B* **1989**, *40*, 3616.

(46) Martínez, L.; Andrade, R.; Birgin, E. G.; Martinez, J. M. Packmol: A Package for Building Initial Configurations for Molecular Dynamics Simulations. *J. Comput. Chem.* **2009**, *30*, 2157−64.

(47) Andolina, C. M.; Williamson, P.; Saidi, W. A. Optimization and Validation of a Deep Learning Cuzr Atomistic Potential: Robust Applications for Crystalline and Amorphous Phases with near-Dft Accuracy. *J. Chem. Phys.* **2020**, *152*, No. 154701.

(48) Plimpton, S. Fast Parallel Algorithms for Short-Range Molecular Dynamics. *J. Comput. Phys.* **1995**, *117*, 1−19.

(49) Hirel, P. Atomsk: A Tool for Manipulating and Converting Atomic Data Files. *Comput. Phys. Comm.* **2015**, *197*, 212−219.

(50) Jain, A.; Ong, S. P.; Hautier, G.; Chen, W.; Richards, W. D.; Dacek, S.; Cholia, S.; Gunter, D.; Skinner, D.; Ceder, G.; et al. Commentary: The Materials Project: A Materials Genome Approach to Accelerating Materials Innovation. *APL Mater.* **2013**, *1*, No. 011002.

(51) Henkelman, G.; Uberuaga, B. P.; Jónsson, H. A Climbing Image Nudged Elastic Band Method for Finding Saddle Points and Minimum Energy Paths. *J. Chem. Phys.* **2000**, *113*, 9901−9904.

(52) Ferrando, R. Stress-Driven Structural Transitions in Bimetallic Nanoparticles. In *Frontiers of Nanoscience*; Bromley, S. T.; Woodley, S. M., Eds.; Elsevier, 2018; Vol. *12*, pp 189−204.

(53) Wulff, G. Xxv. Zur Frage Der Geschwindigkeit Des Wachsthums Und Der Auflösung Der Krystallflächen. *Z. Kristallogr. - Cryst. Mater.* **1901**, *34*, 449.

(54) Bussi, G.; Donadio, D.; Parrinello, M. Canonical Sampling through Velocity Rescaling. *J. Chem. Phys.* **2007**, *126*, No. 014101.

(55) Ahmad, N.; Bon, M.; Passerone, D.; Erni, R. Template-Assisted in Situ Synthesis of Ag@Au Bimetallic Nanostructures Employing Liquid-Phase Transmission Electron Microscopy. *ACS Nano* **2019**, *13*, 13333−13342.

(56) de Boer, F. R.; Boom, R.; Mattens, W. C. M.; Miedema, A. R.; Niessen, A. K. *Cohesion in Metals: Transition Metal Alloys*, 1988; Vol. *1*.

(57) Touloukian, Y. S.; Kirby, R. K.; Taylor, R. E.; Desai, P. D. *Thermal Expansion: Metallic Elements and Alloys*; Plenum: New York, 1975; Vol. *13*, p 1436.

(58) Simmons, G. *Single Crystal Elastic Constants and Calculated Aggregate Properties*; Southern Methodist University: Dallas, Texas, 1965; p 273.

(59) Hill, R. The Elastic Behaviour of a Crystalline Aggregate. *Proc. Phys. Soc., A* **1952**, *65*, 349−354.

(60) Reuss, A. Berechnung Der Fließgrenze Von Mischkristallen Auf Grund Der Plastizitätsbedingung Für Einkristalle. *Z. Angew. Math. Mech.* **1929**, *9*, 49−58.

(61) Voigt, W. *Lehrbuch Der Kristallphysik*; Teubner Leipzig, 1928; Vol. *962*.

(62) Kittel, C.; McEuen, P.; McEuen, P. *Introduction to Solid State Physics*; Wiley: New York, 1996; Vol. *8*.

(63) Fiorentini, V.; Methfessel, M. Extracting Convergent Surface Energies from Slab Calculations. *J. Phys.: Condens. Matter* **1996**, *8*, 6525−6529.

(64) Hofmeister, H. Shape Variations and Anisotropic Growth of Multiply Twinned Nanoparticles. *Z. Kristallogr.* **2009**, *224*, 528−538.

(65) Lohse, S. E.; Burrows, N. D.; Scarabelli, L.; Liz-Marzán, L. M.; Murphy, C. J. Anisotropic Noble Metal Nanocrystal Growth: The Role of Halides. *Chem. Mater.* **2014**, *26*, 34−43.

(66) Jana, N. R. Gram-Scale Synthesis of Soluble, near-Monodisperse Gold Nanorods and Other Anisotropic Nanoparticles. *Small* **2005**, *1*, 875−82.

(67) Lohse, S. E.; Murphy, C. J. The Quest for Shape Control: A History of Gold Nanorod Synthesis. *Chem. Mater.* **2013**, *25*, 1250−1261.

(68) Yu, B. D.; Scheffler, M. Ab Initio Study of Step Formation and Self-Diffusion on Ag(100). *Phys. Rev. B* **1997**, *55*, 13916−13924.

(69) Elkoraychy, E.; Sbiaai, K.; Mazroui, M.; Boughaleb, Y.; Ferrando, R. Numerical Study of Hetero-Adsorption and Diffusion on (100) and (110) Surfaces of Cu, Ag and Au. *Surf. Sci.* **2015**, *635*, 64−69.

(70) Nilekar, A. U.; Ruban, A. V.; Mavrikakis, M. Surface Segregation Energies in Low-Index Open Surfaces of Bimetallic Transition Metal Alloys. *Surf. Sci.* **2009**, *603*, 91−96.

(71) Greeley, J.; Norskov, J. K.; Mavrikakis, M. Electronic Structure and Catalysis on Metal Surfaces. *Annu. Rev. Phys. Chem.* **2002**, *53*, 319−48.

(72) Perkins, L. S.; DePristo, A. E. The Influence of Lattice Distortion on Atomic Self-Diffusion on Fcc (001) Surfaces: Ni, Cu, Pd, Ag. *Surf. Sci.* **1995**, *325*, 169−176.

(73) Surrey, A.; Pohl, D.; Schultz, L.; Rellinghaus, B. Quantitative Measurement of the Surface Self-Diffusion on Au Nanoparticles by Aberration-Corrected Transmission Electron Microscopy. *Nano Lett.* **2012**, *12*, 6071−6077.

(74) Giannozzi, P.; Baroni, S.; Bonini, N.; Calandra, M.; Car, R.; Cavazzoni, C.; Ceresoli, D.; Chiarotti, G. L.; Cococcioni, M.; Dabo, I.; et al. Quantum Espresso: A Modular and Open-Source Software Project for Quantum Simulations of Materials. *J. Phys.: Condens. Matter* **2009**, *21*, No. 395502.

(75) Baletto, F.; Mottet, C.; Ferrando, R. Molecular Dynamics Simulations of Surface Diffusion and Growth on Silver and Gold Clusters. *Surf. Sci.* **2000**, *446*, 31−45.

(76) Roling, L. T.; Mavrikakis, M. Toward Rational Nanoparticle Synthesis: Predicting Surface Intermixing in Bimetallic Alloy Nanocatalysts. *Nanoscale* **2017**, *9*, 15005−15017.

(77) Samal, A. K.; Polavarapu, L.; Rodal-Cedeira, S.; Liz-Marzan, L. M.; Perez-Juste, J.; Pastoriza-Santos, I. Size Tunable Au@Ag Core-Shell Nanoparticles: Synthesis and Surface-Enhanced Raman Scattering Properties. *Langmuir* **2013**, *29*, 15076−82.

(78) Zhang, Q.; Lee, J. Y.; Yang, J.; Boothroyd, C.; Zhang, J. Size and Composition Tunable Ag−Au Alloy Nanoparticles by Replacement Reactions. *Nanotechnology* **2007**, *18*, No. 245605.

https://doi.org/10.1021/acs.jpcc.1c04403
J. Phys. Chem. C 2021, 125, 17438−17447